Eur. Phys. J. B **16**, 169–182 (2000)

THE EUROPEAN PHYSICAL JOURNAL B

EDP Sciences

Molecular dynamics of comminution in ball mills

V. Buchholtz[1], J.A. Freund[2], and T. Pöschel[2,3,a]

[1] Logos Verlag Berlin, Michaelkirchstraße 13, 10179 Berlin, Germany
[2] Humboldt-Universität, Institut für Physik, Invalidenstraße 110, 10115 Berlin, Germany
[3] ICA1, Universität Stuttgart, Pfaffenwaldring 27, 70569 Stuttgart, Germany

Received 19 January 2000

Abstract. We investigate autogenous fragmentation of dry granular material in rotating cylinders using two-dimensional molecular dynamics. By evaluation of spatial force distributions achieved numerically for various rotation velocities we argue that comminution occurs mainly due to the existence of force chains. A statistical analysis of these force chains explains the spatial distribution of comminution efficiency in ball mills as measured experimentally by Rothkegel [1] and Rolf [2]. For animated sequences of our simulations see `http://summa.physik.hu-berlin.de/~kies/mill/bm.html`

PACS. 81.05.Rm Porous materials; granular materials – 83.70.Fn Granular solids

1 Introduction

In the past years molecular dynamics simulations of granular systems – such as sand, fertilizer, grain and others – have been developed towards a reliable tool for an investigation of granular systems. Unlike a few years ago, when physicists started to investigate granular assemblies consisting of just a few hundred spherical granular particles in two dimensions, *e.g.* [3–9], and less than 100 particles in three dimensions, *e.g.* [10], today, owing to the rapid evolution of computer facilities, we are able to simulate complex systems of many thousands of particles in two and three dimensions even accounting for non-spherical grain features.

Due to this progress molecular dynamics of granular systems by now can be applied to the simulation of technologically important processes striving for a better understanding of relevant details of the process and, henceforth, for an optimization of industrial technologies (*e.g.* [11–17]). Molecular simulation techniques, therefore, might develop to a prospective engineering tool partly replacing costly laboratory experiments by "computer experiments".

In the present paper we apply the method of molecular dynamics to the simulation of autogenous dry comminution in a tumbling ball mill [18]. To this end we devised a novel algorithm which accounts for the fragmentation of particles. First we will demonstrate that experimentally known results, in particular those by Rothkegel and Rolf [1,2], can be reproduced up to a good degree of accuracy. We will show that the efficiency of comminution in ball mills is mainly determined by the presence of force chains. Our results will hint at how to improve the efficiency of a milling machinery widely applied in industry.

[a] e-mail: `thorsten@physik.hu-berlin.de`

2 The simulation model

2.1 Molecular dynamics

For the simulation we assumed pairwise interaction forces and applied the model by Cundall and Strack [4] and Haff and Werner [3]: A pair of two-dimensional spherical particles i and j interacts through the force

$$\mathbf{F}_{ij} = F_{ij}^{\mathrm{N}}\,\mathbf{n} + F_{ij}^{\mathrm{T}}\,\mathbf{t}, \tag{1}$$

if their distance is smaller than the sum of their radii $R_i + R_j - |\mathbf{r}_i - \mathbf{r}_j| = \xi_{ij} > 0$. The unit vectors in normal and tangential direction are defined as

$$\mathbf{n} = \mathbf{r}_{ij} / |\mathbf{r}_{ij}| \tag{2}$$

$$\mathbf{t} = \begin{pmatrix} 0 & -1 \\ 1 & 0 \end{pmatrix} \cdot \mathbf{r}_{ij} / |\mathbf{r}_{ij}|\,, \tag{3}$$

with $\mathbf{r}_{ij} \equiv \mathbf{r}_i - \mathbf{r}_j$. The forces in normal and tangential direction are respectively given by

$$F_{ij}^{\mathrm{N}} = Y\xi_{ij} - m_{ij}^{\mathrm{eff}}\,\gamma_{\mathrm{N}}\,\dot{\mathbf{r}}_{ij}\cdot\mathbf{n} \tag{4}$$

$$F_{ij}^{\mathrm{T}} = \mathrm{sign}(v_{ij}^{\mathrm{rel}})\,\min\left(m_{ij}^{\mathrm{eff}}\gamma_{\mathrm{T}}\left|v_{ij}^{\mathrm{rel}}\right|, \mu\left|F_{ij}^{\mathrm{N}}\right|\right) \tag{5}$$

with

$$v_{ij}^{\mathrm{rel}} = \dot{\mathbf{r}}_{ij}\cdot\mathbf{t} + R_i\,\Omega_i + R_j\,\Omega_j \tag{6}$$

$$m_{ij}^{\mathrm{eff}} = \frac{m_i\,m_j}{m_i + m_j}\,\cdot \tag{7}$$

Here R_i, m_i, $\mathbf{r}_i$, $\dot{\mathbf{r}}_i$ and Ω_i are respectively the radius, the mass, the position, the velocity and the rotation velocity of the ith particle. $Y = 8\times10^6$ g s^{-2} is the elastic constant and $\gamma_{\mathrm{N}} = 800$ s^{-1}, $\gamma_{\mathrm{T}} = 3000$ s^{-1} are the parameters of damping in normal and tangential direction. The Coulomb friction constant was assumed to be $\mu = 0.5$. These empirical values which we used throughout all simulations have proven to render realistic behaviour for a typical granular material.

The normal force (4) is composed of an elastic repulsive part and a dissipative part which acts against the direction of motion. For a collision of two-dimensional spheres, *i.e.* disks, the Hertz contact law $F_{ij}^{\mathrm{N}} \sim \xi_{ij}^{3/2}$ [19,20] reduces to [21]

$$\xi_{ij} \sim F_{ij}^{\mathrm{N}} \left(\frac{2}{3} + \ln \frac{4(R_i + R_j)E_{\mathrm{r}}}{F_{ij}^{\mathrm{N}}} \right), \tag{8}$$

where E_{r} is the reduced elastic module, *i.e.* a material constant. Equation (8) provides a relation $\xi = \xi\left(F^{\mathrm{N}}\right)$, however, in the molecular dynamics simulations we need the inverse $F^{\mathrm{N}} = F^{\mathrm{N}}(\xi)$. To calculate the forces due to equation (8) one would have to invert (8) numerically for each particle contact in each time step, *i.e.*, to solve a transcendental equation. Alternatively one could tabulate the function $F^{\mathrm{N}}(\xi)$ but due to large force gradients, in particular in the instant of contact, we have to simulate with double precision accuracy. Therefore, the table would be extremely large. Apart from the small logarithmic term $-F_{ij}^{\mathrm{N}} \ln F_{ij}^{\mathrm{N}}$ in equation (8) one finds that the force is proportional to the compression ξ_{ij}. Therefore, in our simulations we used the linear law (4) which is a good approximation in the force interval of interest.

Equation (6) describes the relative velocity of the particle surfaces at the point of contact which results from both the tangential part of the relative particle velocity and the velocity of particle spin.

The Coulomb friction law is taken into account in equation (5): If the tangential force of two colliding particles exceeds μ times the normal force the particles slide upon each other feeling constant friction. In this way the Coulomb law formulates a maximum transferable shear force.

As numerical integration scheme we used the Gear predictor-corrector method of sixth order (*e.g.* [22]).

Let us remark that there exist various models with diverse descriptions of the interaction forces, *e.g.* [23]. In three-dimensional calculations it is crucial that the dissipative term in (4) is proportional to $\sqrt{\xi}\dot{\xi}$ [24] (in viscoelastic approximation). In three dimensions the used term $\sim \dot{\xi}$ in equation (4) yields wrong results [23,25].

Another class of molecular dynamics are event-driven simulations, *e.g.* [26] which require much less numerical effort than the method described above (force-driven molecular dynamics). In event-driven simulations one does not integrate the equations of motion explicitly but rather expresses the loss of mechanical energy in normal and tangential direction due to a collision *via* coefficients of restitution ϵ^{N} and ϵ^{T} both of which can be determined from the material properties of the particles [24,27]. Besides some conceptional difficulties which can be overcome by applying numerical tricks [28] these algorithms are only applicable in case the duration of collisions is negligible in comparison with the mean free flight time, *i.e.* the time a particle moves without interaction. In this limit collisions can be assumed as instantaneous events. Moreover, this implies that three-particle interactions are very rare events. However, in the system under study, namely the ball mill, this premise does not hold because the majority of particles permanently is in close contact with neighbouring particles.

2.2 Fragmentation probability of grains

It can be observed in experiments that different particles of identical size and material vary with respect to their tensile strengths. That means when compressing particles of a sample by applying a fixed force only a fraction of the sample actually will break. For a sufficiently large sample this fraction can be rephrased in terms of a fracture probability.

The reason for this different behaviour can be explained by the existence of flaws which provide sites for stress concentration and the initiation of a crack which, subsequently, propagates through the material. These flaws are distributed throughout the whole volume, however, several investigations have revealed that surface flaws activated by high tensile stress play the dominant role for the initiation of a crack [29]. Hence, the fracture probability is intimately related to the statistical distribution of surface flaws and the resulting stress distribution over the particle's surface.

Starting from some plausible assumptions concerning the flaw distribution and the behaviour of the material the fracture probability P of a single particle can be derived employing statistical reasoning. A particle of radius R, subjected to a force which stores the specific elastic energy $W_m = W/m$, will break with probability [30]

$$P(R, W_m) \sim 1 - \exp\left(-cR^2 W_m^z\right). \tag{9}$$

Here, c and z are material constants. The original derivation (considering rods of a brittle material) goes back to Weibull [31]. This simple law has proven in practice by fitting various experimental data. The constants c and z can be extracted from measurements when plotting $[\ln\ln(1-P)^{-1}]$ *vs.* $[\ln W_m]$. Typical values of z are found to lie in the range 1.5, ..., 2.5.

Notice that in agreement with experimental results the term R^2 in the exponent (for fixed W_m) in general predicts an anticorrelation between particle size and resistance to breakage. Clearly, this fact is rooted in the diminished probability to find a sufficiently large flaw on a smaller surface.

For spherical particles (or, more generally, for particles having convex surface), assuming linear elastic behaviour, Hertz-theory [19,20] can be employed to derive a relation

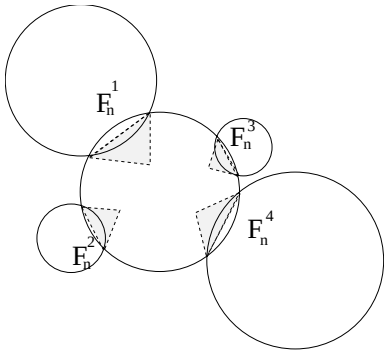

Fig. 1. A typical situation of one particle being compressed by four impacting particles. The forces are considered as independent stress sources. Therefore, in simulations we evaluated only the maximum of all exerted forces to compute the fracture probability $P(R, W_m)$.

between the elastic energy W stored in a sphere and the exerted repulsive contact force F

$$W = \frac{2}{5}\xi F = \frac{2}{5}\left(\frac{D^2F^5}{R}\right)^{\frac{1}{3}}, \tag{10}$$

where ξ quantifies the particle's deformation and D is another material constant (expressed by the Poisson ratio and constant of elasticity) [19,20]. It should be kept in mind that formula (10) remains valid in the linear elastic regime only.

Applied to our simulation of ball mills we make use of these laws in the following way: Consider the situation sketched in Figure 1: A particle placed in the centre is compressed by four impacting particles.

The highest compressive stress occurs around the contact point; a fact well-known to engineers [32] and also found in numerical simulations [33,34]. Hence, the fracture probability of the centre particle is linked to the probability of finding a flaw of sufficient size in the very vicinity of any of the four contact regions. Thus, the action of different impacting particles can be regarded as independent stress sources. That means we consider the elastic energy stored by each impacting particle separately, calculate the related fracture probability according to formulae (9, 10) as a function of the particle's size and the maximum of all acting normal forces F^{N}

$$P(R, F^{\mathrm{N}}) \sim 1 - \exp\left(-\tilde{c}R^{\left(2-z\frac{10}{3}\right)}\left(F^{\mathrm{N}}\right)^{\frac{5z}{3}}\right), \tag{11}$$

and actually decide the question of breakage by subsequently drawing a random number for each of the contact sites.

The constant $\tilde{c}$ is related to the empirical constant c in equation (9); the precise connection is elaborated by inserting equation (10) into (9) and expressing m by the particle radius $m \propto R^3$.

Up to this point we discussed the fracture probability for three-dimensional spheres. In our simulations we modelled two-dimensional spheres, *i.e.* circular discs of unique thickness L. The fracture probability corresponding to equation (11) can be obtained in analogy to (9) yielding

$$P(R, W_m) \sim 1 - \exp\left(-cRLW_m^z\right). \tag{12}$$

Note that the surface of a sphere $\propto R^2$ has to be replaced by the surface of a cylinder $\propto RL$ (excluding top and bottom wall). Correspondingly equation (10) turns into $\xi = YF^{\mathrm{N}}$ and, hence, the stored elastic energy for spheres has to be replaced by

$$W = \frac{1}{2}\xi F^{\mathrm{N}} = \frac{(F^{\mathrm{N}})^2}{2Y} \sim (F^{\mathrm{N}})^2. \tag{13}$$

Taking into account that the mass of a cylinder is proportional $\propto R^2$, one obtains

$$P(R, F^{\mathrm{N}}) \sim 1 - \exp\left(-\tilde{c}R\left[\frac{(F^{\mathrm{N}})^2}{R^2}\right]^z\right). \tag{14}$$

In Section 3 we will motivate the choice $z = 2$. With this specification one finally arrives at the following expression for the fracture probability

$$P(R, F^{\mathrm{N}}) \sim 1 - \exp\left(-\tilde{c}R^{-3}\left(F^{\mathrm{N}}\right)^4\right). \tag{15}$$

3 Fragment size distribution

Once a flaw has been activated it forms an initial crack which rapidly propagates through the particle. Typical crack velocities in the range of 1500 m/s have been measured [29]. The formation of a variety of differently sized fragments occurs by virtue of branching cascades. Branching is governed by a balance between the energy release rate G and the so-called crack resistivity B [29] the latter accounting for the creation of new surfaces. Because of the extremely short duration of the rupture process one can safely neglect external energetic contributions to this energy balance. The energy release rate G depends on the crack velocity and the crack length whereas the crack resistivity B depends on the crack velocity and on the number of branches. Due to a maximal crack velocity, *viz.* the speed of sound, the balance between both terms requires the formation of new cracks. From these considerations it can be shown [29] that the fragment size distribution (cumulative mass distribution) Q is a function of the product $R_{\mathrm{f}}\, W_m$, where R_{f} denotes the fragment size, *i.e.* $Q = Q(R_{\mathrm{f}}\, W_m)$.

Experimental evidence [30] for a scaling law $Q \sim R_{\mathrm{f}}^{\beta}$ is in agreement with the well-known empirical Schuhmann law [35]

$$Q \sim \left(\frac{R_{\mathrm{f}}}{k}\right)^{\beta}, \tag{16}$$

which itself can be regarded as an approximation of the Rosin-Rammler law [36]

$$Q \sim 1 - \exp\left[-\left(\frac{R_{\mathrm{f}}}{k}\right)^{\beta}\right]. \tag{17}$$

The variable k has the dimension of a length and, thus, can only be identified with the size of the original particle.

A rigorous derivation of equation (17) – compatible with an exponent $\beta = 1$ – starting from rather mild assumptions and applying Poisson statistics was performed by Gilvary [37] (see also [38]).

It has to be mentioned that the derived laws (16, 17) describe the distribution of fragments only below a certain size (endoclastic *vs.* exoclastic distribution [37]). For the largest fragments an equivalently well-defined quantitative statement does not exist. The deviation between theoretical predictions and experimental observations typically occurs for grains which together collect about 75–90% of the total mass [29]. Moreover, some diverging theoretical mean values can be understood from the fact that the assumption of equidistributed flaws on all length scales neglects the effect of flaw depletion applying to tiny fragments. Flaw depletion thus sets a lower bound to the range of applicability. Insofar the size of fragments which is satisfactorily described by the distributions (16, 17) is restricted to the intermediate range.

When fitting both the more refined Rosin-Rammler law (17) and the simplified Schuhmann law (16) to diverse experimental data it was found that in some situations the Rosin-Rammler law proved superior [29] (mill products [38]) whereas in other cases (specimen fractured in gelatin [38]) the Schuhmann law was even more adequate.

Finally, we mention the *population balance model* [39] which assumes that the fragment size distribution can be normalized to the initial particle size, *i.e.* $Q = Q(R_\mathrm{f}/R)$. This assumption is based on empirical observations. Moreover, its central assertion can also be derived when starting from a Weibull exponent $z = 2$ and applying statistical reasoning similar to the one sketched above.

In our simulations we employed the Rosin-Rammler law (17) with $k = R$ and an exponent $\beta = 1$. Since experimental data have shown the mean dimension of the largest fragment to be roughly 75% of the original particle size [38], *i.e.* $R_\mathrm{f}^\mathrm{max} = \frac{3}{4}R$, the normalized fragment size distribution simply reads

$$Q\left(\frac{R_\mathrm{f}}{R}\right) = \frac{1 - \exp\left(-\dfrac{R_\mathrm{f}}{R}\right)}{1 - \exp\left(-\dfrac{3}{4}\right)} \cdot \tag{18}$$

3.1 Molecular dynamics modelling of fragmentation

In the present study we exclusively utilize spherical particles (disks), which means that also the fragments of a disrupted particle must be spherical. The single fracture statistics, as discussed in Section 3, is put into practice by dismembering a cracking disk into two fragments. Whereas the size of one fragment is chosen in accordance with the Rosin-Rammler law the size of the second one is determined by mass conservation, *i.e.* for two-dimensional particles by area conservation.

In the majority of situations a breaking particle is closely surrounded by neighbouring ones. Hence, in general, it will be impossible to place the two fragments avoiding an overlap. However, since a considerable overlap corresponds to a situation of extreme compression an unrealistically strong repulsive normal force (4) together with an exceptional deformation energy would be the consequence. We bypassed this problem by modifying the interaction between the two fragments in the following way: Up to the moment of first complete separation of two such fragments i and j the normal force (4) at the $(k+1)$st time step is replaced by

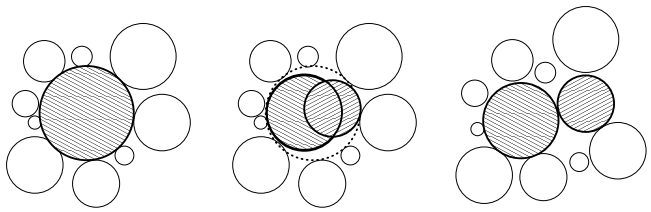

Fig. 2. Sketch of the particle fragmentation procedure. Immediately after the fragmentation the particles must overlap due to mismatch of geometry of the spherical fragments (middle), a small repulsive force helps to overcome this unphysical transient situation.

$$F_{ij}^\mathrm{N} = \begin{cases} Y\xi_{ij}^*(k) - m_{ij}^\mathrm{eff}\,\gamma_\mathrm{N}\,(\dot{\mathbf{r}}_i - \dot{\mathbf{r}}_j)\cdot\mathbf{n} \\ \qquad\qquad\qquad \text{if} \quad (\dot{\mathbf{r}}_i - \dot{\mathbf{r}}_j)\cdot\mathbf{n} < 0 \\ \epsilon \qquad\qquad\qquad \text{otherwise} \end{cases} \tag{19}$$

with

$$\xi_{ij}^*(k) = |\mathbf{r}_i(k-1) - \mathbf{r}_j(k-1)| - |\mathbf{r}_i(k) - \mathbf{r}_j(k)|\,. \tag{20}$$

This means that the two fragments, on the one hand, resist to further compression like standard particles and, on the other hand, experience a small repelling force ϵ which drives them apart. The repelling force is chosen sufficiently small in order to suppress unphysical energy gain of the system; this means that the unavoidable energy, which due to this force is pumped into the system anyhow, must be negligible in comparison with the mean kinetic energy of the grains. After the moment of first complete separation of the two fragments they also interact in the standard way, as dictated by equation (1). Of course, the interaction of two such fragments with all other particles is never modified. By trimming of ϵ we could not only suppress the elastic energy gain but also evidenced that the period requiring a modified interaction force was comparatively short. The procedure of fragmentation is sketched in Figure 2. We want to mention that multiple fragmentation, *i.e.* further fragmentation of the fragments is included in the model and is frequently observed in simulations.

Let us remark that our algorithm was flexible enough to include multiple fracture events: By this we mean the observation that a fragment was apt to break itself even before its first complete separation from its original twin fragment.

An animated sequence of fragmentation can be found in the internet under

`http://summa.physik.hu-berlin.de/~kies/mill/bm.html`

Finally, we mention that the proposed algorithm is not the only way to model particle fragmentation. An alternative algorithm has been put forward by Åström and Herrmann [40].

3.2 Specification of the model system

As depicted in Figure 3 the cylindrical wall of our system has been modelled by an ensemble of spheres possessing the same material constants as the grains inside the container. However, the motion of wall spheres is not affected by impacts but, instead, strictly governed by the continuous rotation of the cylinder. Moreover, in spite of identical elastic and dissipative constants the wall particles were considered to be much harder so they never would break.

A suitable size distribution of wall particles generates the effect of surface roughness. This type of modelling has been used in several numerical simulations and is also used in experiments to guarantee well-defined boundary properties. The wall particles have been placed along the circumference of the cylinder. Just like in realistic ball mills we evenly distributed 16 toolbars along the inner periphery of the cylinder which serve to lift particles and thus prevent them from sliding downhill. We composed the toolbars again from a collection of rigid spheres. As reported in literature [32] the maximum milling efficiency is achieved for a filling degree, *i.e.* the ratio of material and container volume, of ca. 40%.

The simulation results to be presented in the next section have been done with a system consisting on average of about 1000 particles. Due to fragmentation the number of particles was not constant, *i.e.* the particle number fluctuates. The container was modeled by about 500 wall particles as described above.

Initially the spheres which model the grist were randomly positioned inside the container avoiding any overlap. This artificial initial condition had to be relaxed by evolution of the system. In this way we achieved a realistic configuration for any chosen rotation velocity. Obviously the typical asymptotic configuration depends on the rotation frequency ν, therefore, we started our numerical monitoring only after transients had died out. In Figure 4 we present snapshots of typical configurations depending on four different rotation frequencies.

In technologically relevant ball mills there is a continuous transport of raw material into the mill and of milled material out of the device. In most industrial applications this exchange of raw material and final product is accomplished by axial transport (z-direction) of material. Of course, with our two-dimensional model we cannot account for axial transport, therefore, we simulated the material exchange in continuous operation mode in the following way: Whenever fragments were generated whose size dropped below a minimum we removed them from the container. After exact bookkeeping of the mass of removed "dust" particles we reinserted a big particle when the accumulated dust mass exceeded an upper threshold, of course, obeying mass conservation. In this way we conserved the average filling level throughout the simulation and, thus, could reach a steady state of the continuous operation mode.

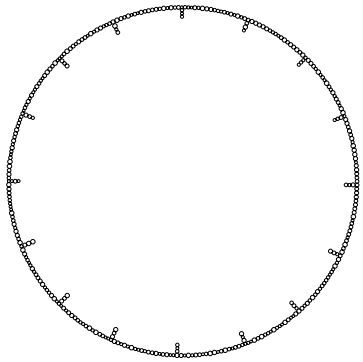

Fig. 3. The cylindrical container is modeled by particles placed along the circumference of the container. Roughness is taken into account by stochastic variation of the sizes of these particles.

4 Simulation results

4.1 Mass distributions

As a first result we studied the frequency dependent fragment size distribution. This distribution is not necessarily equal to the distribution of Section 3, which was the result of single fracture experiments.

It is known [41–43] that for an arbitrary fracture mechanism, which hierarchically is applied on all length scales, one will always generate a log-normal distribution of fragment sizes; this assertion is a pure consequence of the central limit theorem. However, in our modelling the ball mill is operated as an open system, *i.e.* there is a particle flow into and out of the mill. Therefore, analyzing the asymptotic size distribution is also of theoretical interest.

Furthermore, the explicit knowledge of the distribution plays also a practical role, because from that knowledge one can decide whether a multi-level fragmentation process is to be preferred to a single-level one or *vice versa*. A multi-level process can be either a distribution of the comminution process to several ball mills, where each is filled with granular material of a specified narrow size distribution, or a spatial separation of material of different size in one mill.

Figure 5 shows the differential fragment size distribution, *i.e.* the mass fraction of all particles with size within a certain interval, for four different rotational frequencies. The black circles in each column correspond to measurements at different times and thus reflect the temporal variance. The time period of each simulation was 10 seconds real time (beyond transients).

Obviously the lowest curve (2.5 Hz) changes only very weakly during the simulation, which can be interpreted

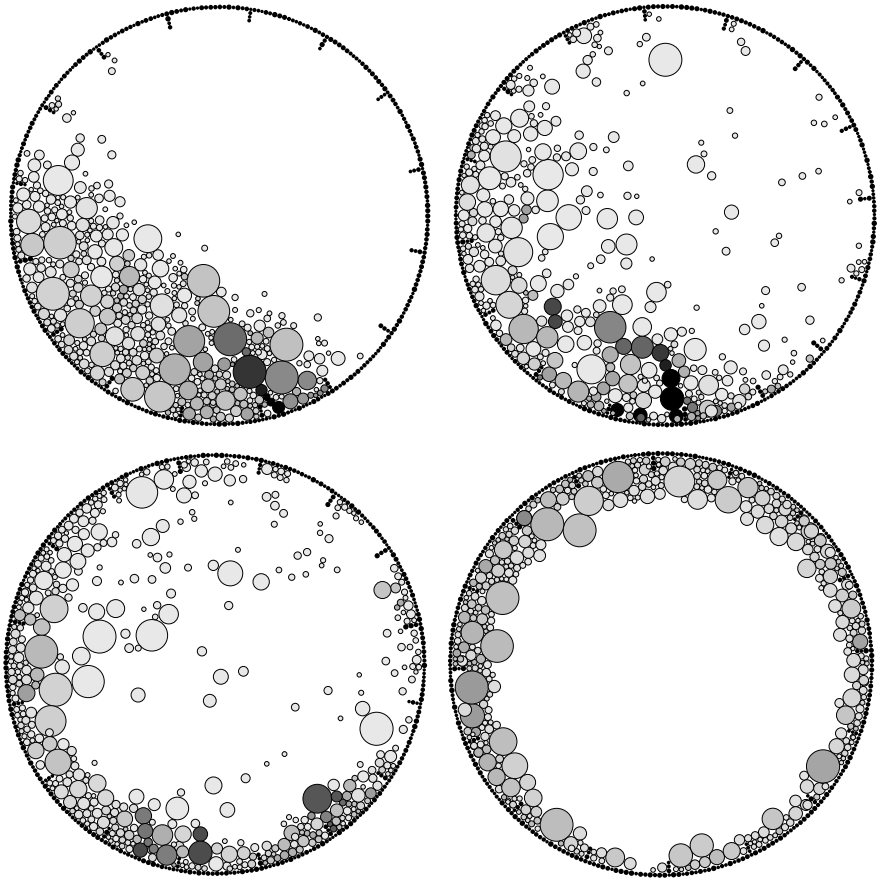

Fig. 4. Typical dynamical configurations depend on the rotation speed: 0.5 Hz (top left), 1.0 Hz (top right), 1.25 Hz (bottom left), 2.5 Hz (bottom right). Grey scale codes the instantaneous maximum compression (normal force) experienced by each particle through contact with its neighbours (light: small normal force, dark: large force). Obviously the largest forces occur in the range of intermediate rotation velocities (1.0 Hz, 1.25 Hz). Moreover, we identify the location of largest forces which can initialize fragmentation to be close to the bottom of the rotating cylinder. This important observation will be discussed in detail in Section 5.

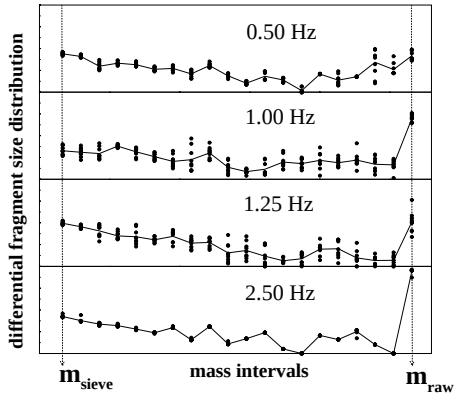

Fig. 5. The differential fragment size distribution for different rotation velocities. The black circles represent the values for a fixed mass interval at different times. The variance of the circles illustrates fluctuations of the distribution. The solid lines are tracing the averages of each interval. The left border of the scale is fixed by the size of the sieve (m_{sieve}), the right border by the size of the refilled big grains (m_{raw}).

as a low rate of fragmentation. This curve – and with restrictions also the top curve (0.5 Hz) – is determined by the initialization. Unfortunately, the middle curves are not significantly different, which mainly is a consequence of the short simulation time (10 seconds). To answer the interesting questions (theoretical distribution, multi-level process) it will be necessary to simulate considerably longer time periods.

4.2 Optimization of the efficiency

In the context of industrial applications the notion of efficiency mainly focuses on the aspects of maximum comminution rate and, perhaps, of power consumption. There are many free parameters which can be varied to maximize the efficiency: speed of rotation, filling degree, size distribution, cylinder diameter, grist size distribution, various mill types, etc.

In our analysis we investigated the dependence of the comminution rate on the speed of rotation. In order

to compare our numerical results with experimental data we normalized quantities in the following way: The speed of rotation is normalized to the velocity $n_c = \sqrt{g/M}(2\pi)^{-1}$ for which the centrifugal force balances the gravitational force whereas the comminution rate is normalized to its measured maximum. The result of our simulation is plotted in Figure 6 using filled circles and dashed line. Clearly, a maximum occurs around $n \approx n_c$ whereas the rate rapidly diminishes for larger or smaller velocities.

The full line in Figure 6 depicts a similar curve following from experiments. The curve shows the relative power consumption as a function of the normalized speed of rotation. Qualitatively both curves are in good agreement; systematic deviations can be explained by the following observation: Strictly speaking both curves relate to different physical quantities. The fraction rate only accounts for the energy dissipated through fractures while the experimental curve includes all dissipative processes, for instance friction between grains, friction between the grains and the wall, dissipative impacts, heating, etc.). As a consequence, the curve for the simulation should be found below the experimental curve. Moreover, from the same reasoning it is also clear that observed deviations are minor if the main portion of the overall dissipated energy results from the fractures, *i.e.* around the maximum.

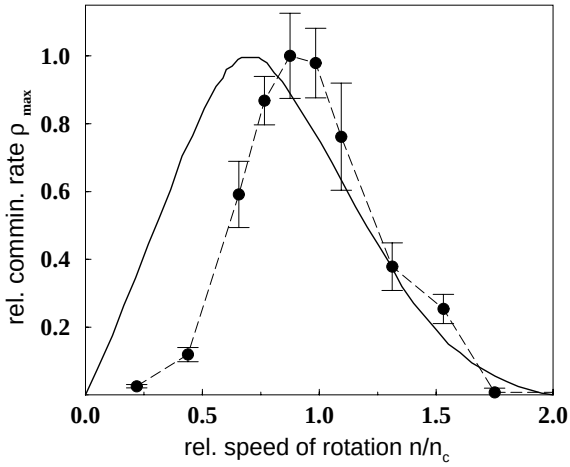

Fig. 6. The dependence of the fraction rate on the rescaled rotation velocity, simulation (filled circles plus dashed line) and experiment (full line) taken from [32] (original in [44]). The error bars for the simulation visualize the fluctuations during the simulation period of approximately 10 seconds real time.

4.3 Preferred fragmentation locations

The series of pictures in Figure 7 illustrates the spatial distribution of fragmentation locations for four different rotation velocities. We restricted our presentation to the most important lower right segment of the ball mill (clockwise rotation). To compute this distribution the coordinates of breaking particles were stored during the simulation. After the simulation the fraction of all fragmentation events occurring at places inside little cells (coarse graining) was computed. In Figure 7 grey values code the frequency: dark means high frequency and light low frequency respectively.

In the bottom right figure one finds a few fragmentation events near the cylinder wall. The restriction to medium-grey values results from the fact, that the rare events are equidistributed across the inner perimeter.

The predominance of rather light grey (or even white) pixels in the rest of the figures hints at regions where fragmentation events are rare as compared to the sparse medium-grey to dark pixels which indicate regions of high fracture probability. The observation that most fragmentation events occur deep inside the material and not near the surface, which is heavily agitated by impacts, is, at first sight, somewhat counter-intuitive. An explanation for this fact will follow from a closer analysis of the local pressure concentration in the next section.

5 Spatial distribution of pressure in ball mills

In this chapter we will dwell on the physical origin of the unusual pressure distribution [45] measured in experiments.

As can be concluded from Figures 7 and 8, the majority of fragmentation events does not occur near the free surface of the granular material but deep inside the material near to the walls. This strange behaviour was observed already in experiments by Rothkegel and Rolf [1,2] in two-dimensional model mills. They used instrumented balls which emitted a flash of light whenever the strain exceeded a fixed threshold. The positions of recorded flashes were digitized and from the statistics of these data they inferred the stationary strain distribution inside the ball mill. For various threshold values they always found the peak strain deep inside the material (see Fig. 8). This was surprising because inside the material relative grain velocities are rather low in comparison with relative velocities at the surface.

This experimental finding, together with its validation by our simulation (see the previous section), calls for an explanation. We will solve this challenging, so far open question using the powerful possibilities of molecular dynamics, namely the option to monitor physical quantities which are hardly accessible through experiments.

In the following simulations we ignored fragmentation events – which are not relevant for our explanation – simply for the sake of computational efficiency, so we could afford longer simulation time. This time the radius of the two-dimensional ball mill was set to $M = 4$ cm. The mill was filled with $N = 800$ spherical grains with radii equally distributed in the interval [0.05, 0.11] cm. We performed simulations with three different rotation velocities $\Omega_{\rm I} = 2$ Hz, $\Omega_{\rm II} = 10$ Hz and $\Omega_{\rm III} = 19$ Hz.

Figure 9 shows snapshots of our performed simulations. The pictures in the top row are taken form a simulation with rotation velocity $\Omega = \Omega_{\rm I}$. The velocity is sufficient to observe a continuous flow at the surface. The surface shape is similar to a plane. The regime with discontinuous flow (for lower rotation velocities) will not

Fig. 7. Spatial distribution of fragmentation locations for different rotation velocities: 0.5 Hz, 1.0 Hz, 1.25 Hz, 2.5 Hz (from top left to bottom right). Grey values code the frequency of fragmentation in a certain region (cell), dark meaning high frequency and light low frequency respectively. Preferred fragmentation regions are found near the bottom of the mill, *i.e.* deep inside the granular material. This observation is in good agreement with experimental results and the results from Section 5.

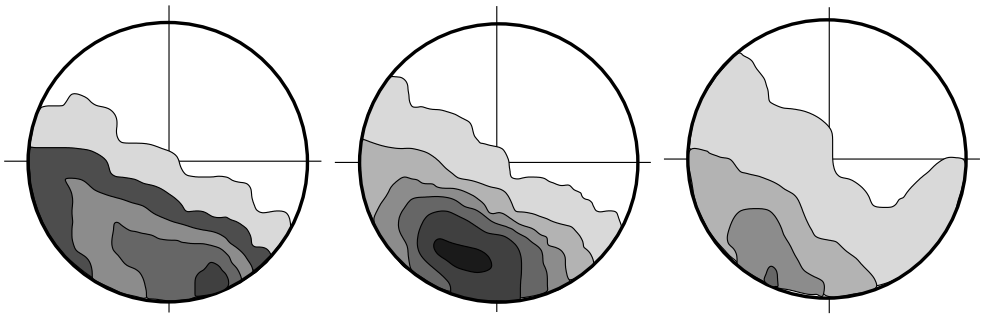

Fig. 8. Spatial distribution of the strain for different rotation velocities and filling grades. Again, grey levels code strain values. The regions of maximal strain are located inside the material. This figure is redrawn from reference [1].

be investigated in this paper, because it is not relevant for technological applications. For a detailed discussion of the interesting observations at the transition between continuous and stick-slip flow we refer to the work by Rajchenbach [46].

The picture in the middle row of Figure 9 depicts snapshots of a simulation with $\Omega = \Omega_{\mathrm{II}}$. The surface of the material no longer shapes a plain but the grains fall down a steep slope hitting a flat surface.

The bottom row of Figure 9 exhibits the snapshot of a simulation with the highest rotation velocity $\Omega = \Omega_{\mathrm{III}}$. Here the grains are carried away with the fast rotation of the cylinder. Beyond a certain point they are likely to loose contact with the wall and follow a free parabola before impacting back down on the surface.

Moreover, the snapshots of Figure 9 provide an intuitive understanding, what mechanism is responsible for the pressure distribution mentioned above. Again, grey values in these pictures code the local pressure P_i acting on grain i given by

$$P_i = \sum_j F_{ij}^{\mathrm{N}}. \tag{21}$$

The index j is running over all particles which are in contact with grain i. Dark circles denote high pressure, light spheres low pressure.

Obviously many of the heavier stressed particles are deep inside the material, which is in good agreement with the experimental observation by Rothkegel and Rolf [1,2]. Most importantly, the pictures reveal that grains experiencing peak stress often form linear structures. In the following we focus on the development and the properties of such force chains. By numerical analysis we will prove that those force chains are the crucial physical reason for the observed pressure distribution.

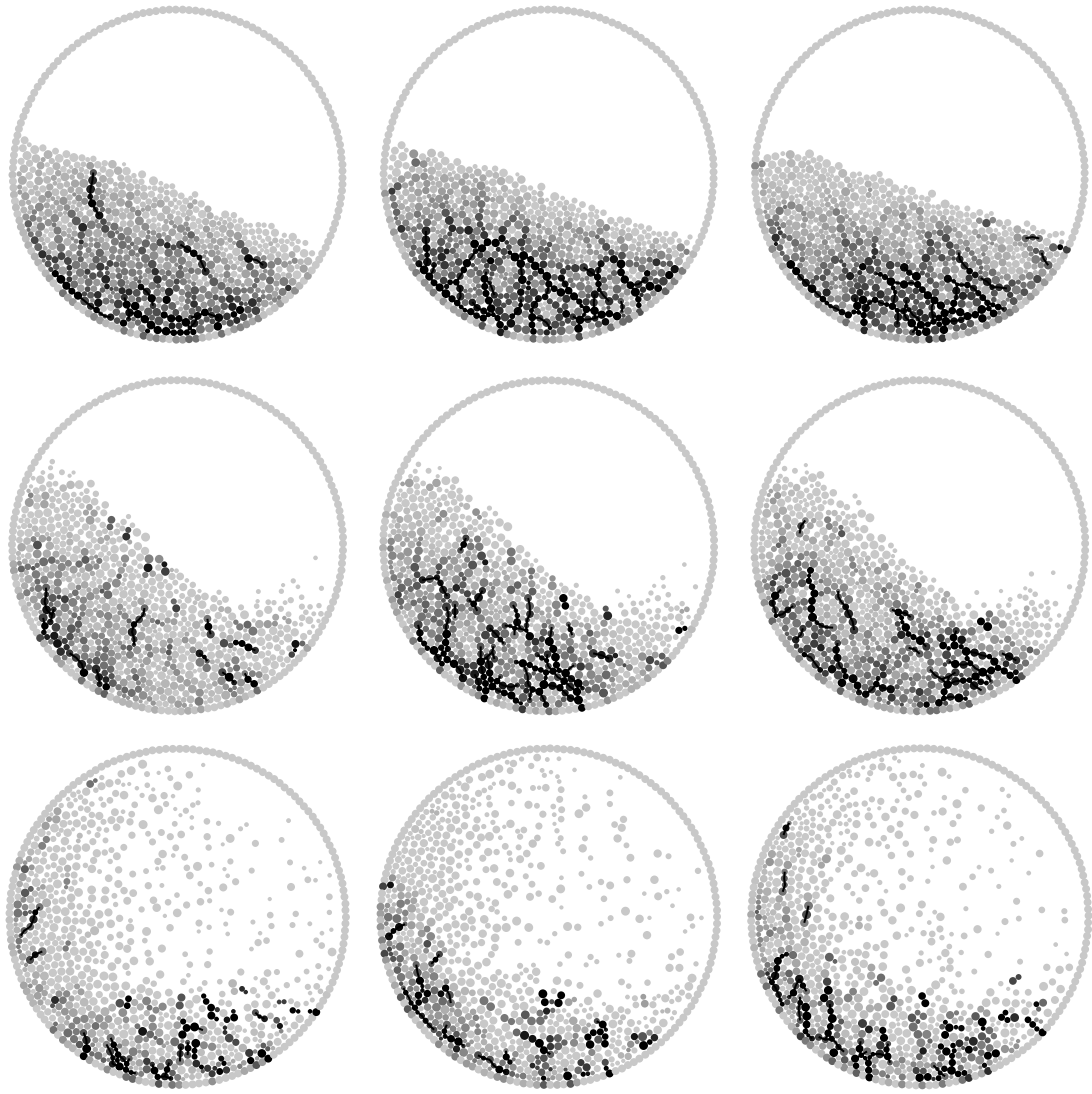

Fig. 9. Snapshots of the simulation for different rotation velocities. Grey values code the local pressure P_i (see text). Linear segments connect grains belonging to a force chain. $\Omega_{\mathrm{I}} = 2$ Hz (top), $\Omega_{\mathrm{II}} = 10$ Hz (middle), $\Omega_{\mathrm{III}} = 19$ Hz (bottom).

We defined force chains by a set of three self-evident conditions: Grains i, j and k are considered to be members of the same force chain if:

1) particles i, j and j, k are next neighbours,
2) the pressure acting on each of the grains exceeds a certain threshold ($P_i > 1000$ g cm s^{-2}),
3) the connecting lines between i, j and j, k form an angle larger than 150°, *i.e.* the centres of three grains almost fall on a line.

These three conditions are evaluated by a computer algorithm. In Figure 9 all grains belonging to a force chain are graphically connected by lines.

We see that most of the harder stressed grains could be assigned to a force chain. From this we conclude that the main part of the static and dynamic pressure propagates along the force chains. The pressure acting on a highly stressed grain inside a force chain is up to 100 times larger as compared to the average pressure of the neighbouring grains not belonging to a force chain, *i.e.* the force distribution is strongly inhomogeneous.

The development of such force chains is not restricted to grains in a ball mill but has been observed in different granular systems by various experimentalists [47–50] and numerically [51–53]. It could be shown, that one of the granular phases is characterized by the observation of force chains [52]. From this one might conclude that the occurrence of force chains is an inherent feature of all granular matter, which may substantially contribute to its specific characteristics.

Figure 10 comprises six plots which come in three pairs; the lower plot of each pair always depicts the frequency distribution of force chains whereas the related upper one presents the (statistically evaluated) maximal pressure both as a function of the length L of a force chain (which is nothing but the number of particles belonging

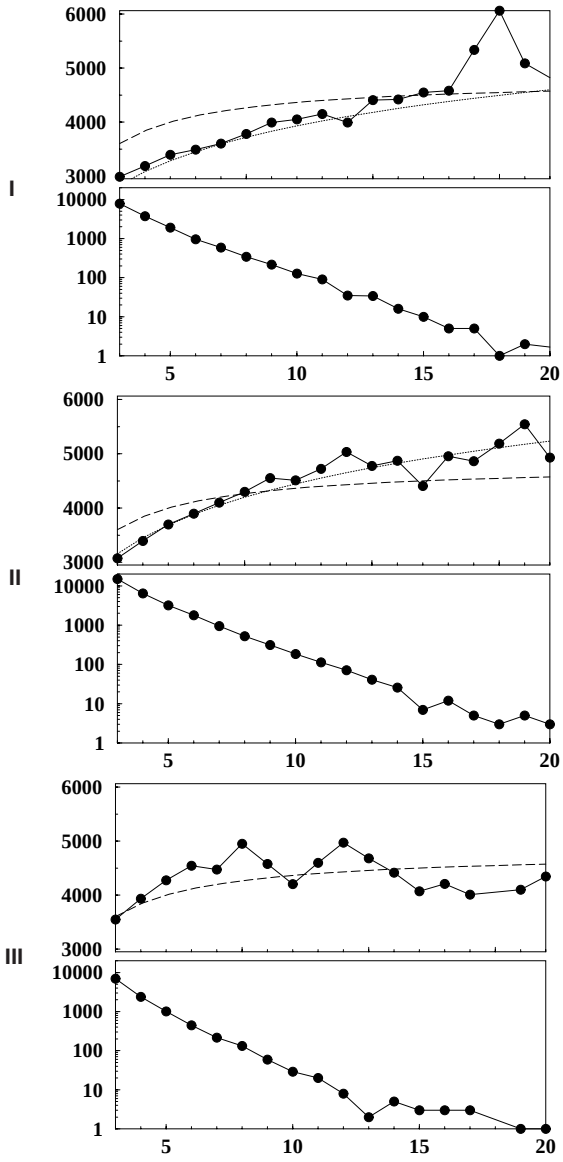

Fig. 10. Within each pair of the triplet (I, II, III) the lower plot presents the frequency distribution whereas the upper one shows the maximal pressure inside a force chain both as a function of its length L (abscissa for all plots). $\Omega_{\mathrm{I}} = 2$ Hz (top), $\Omega_{\mathrm{II}} = 10$ Hz (center), $\Omega_{\mathrm{III}} = 19$ Hz (bottom) (explanation of lines see text).

to the chain). These pairs are shown for three different rotation velocities varying from Ω_{I} (top) to Ω_{III} (bottom).

The frequency of a force chain drops exponentially with increasing length L. For the highest rotation velocity (Ω_{III}) the statistics becomes unreliable for chains longer than $L = 13$. This behaviour, which is in contrast to observations for slower measured rotations, is due to the higher energy input, which causes a decompactification of the material.

Concerning the earlier mentioned spatial strain distribution the *maximal* pressure measured in each force chain is of paramount interest rather than the *average* pressure in a force chain (see Sect. 2.2). For lower rotation velocities Ω_{I} and Ω_{II} a monotonous increase of the maximal pressure with the length L can be observed. For a discussion of these curves one has to take into account that the pairs of plots in Figure 10 do *not* constitute independent quantities. Choosing a sample of L particles from an ensemble of particles on which forces with a given distribution are acting, the maximal force in this sample will increase with increasing L. Therefore, in order to prove significance, the result in Figure 10 has to be weighted against this purely statistical effect.

The probability to measure a maximal pressure $P^{\max}$ in the interval $P^{\max} \in [x; x + \mathrm{d}x]$ in a sample of size L is equal to the probability that all particles feel a pressure $P < x + \mathrm{d}x$ minus the probability that all L particles feel a pressure $P < x$.

$$p_L(P^{\max} \in [x; x+\mathrm{d}x]) = [p(P < x+\mathrm{d}x)]^L - [p(P < x)]^L. \tag{22}$$

Assuming equally distributed pressures $P \in [0 : P_m]$, $p(P < x)$ means

$$p(P < x) = \int_0^x \frac{1}{P_m} \mathrm{d}x' = \frac{x}{P_m} \cdot \tag{23}$$

By inserting equation (23) into equation (22), one finds in first order of $\mathrm{d}x$

$$p_L(P^{\max} \in [x; x + \mathrm{d}x]) = \frac{1}{(P_m)^L} L\, x^{L-1} \mathrm{d}x. \tag{24}$$

Therefore, the average maximal pressure as a function of sample size L is given by

$$\begin{aligned} \langle P^{\max}(L) \rangle &= \frac{1}{(P_m)^L} \int_0^{P_m} x\, L\, x^{L-1} \mathrm{d}x \\ &= \frac{1}{(P_m)^L} \frac{L}{L+1} P_m^{L+1} \\ &= \frac{L}{L+1} P_m. \end{aligned} \tag{25}$$

The dashed lines in Figure 10 show this statistical effect for $P^{\max}$ with $P_m = 4800$ g cm s^{-2}. Obviously, these curves do not reach up to our numerical data of the top and center figure; especially for larger L the dashed line falls far below. The numerical data points in the bottom figure (high rotation velocity) to some extent coincide with the dashed curve, which only represents the statistical effect discussed above. Hence, we can conclude that for lower velocities the maximum stress significantly concentrates within long force chains whereas for high rotation velocities a significant effect of force chains is not evident.

From experimental and numerical results (for instance [49,54,55]) it is known, that the observation of force chains is connected to a strongly inhomogeneous pressure distribution. The distribution is essentially an exponentially

decreasing function with increasing pressure. A simplified expression for this distribution is given by

$$p(P) = a\,\exp\{-a\,P\}. \tag{26}$$

In analogy to equation (23) the probability to measure a pressure $P < x$ is given by

$$p(P<x) = \int_0^x a\,\exp\{-a\,x'\}\mathrm{d}x' = 1-\exp\{-a\,x\}. \tag{27}$$

Inserting this into equation (22) we obtain in first order of $\mathrm{d}x$

$$\begin{aligned} p_L(P^{\max}\in[x;x+\mathrm{d}x]) &= \left(1-\mathrm{e}^{-a(x+\mathrm{d}x)}\right)^L - \left(1-\mathrm{e}^{-a\,x}\right)^L \\ &= L(1-\mathrm{e}^{-a\,x})^{L-1}\mathrm{e}^{-a\,x}a\,\mathrm{d}x. \end{aligned} \tag{28}$$

The average of the maximal pressure can be calculated by integrating

$$\begin{aligned} \langle P^{\max}(L)\rangle &= \int_0^\infty x\,L\left(1-\mathrm{e}^{-a\,x}\right)^{L-1}\mathrm{e}^{-a\,x}a\,\mathrm{d}x = \\ &\lim_{N\to\infty}\left\{x\,\left(1-\mathrm{e}^{-a\,x}\right)^L\Big|_0^{\mathrm{N}} - \int_0^{\mathrm{N}}\left(1-\mathrm{e}^{-a\,x}\right)^L\mathrm{d}x\right\}. \end{aligned} \tag{29}$$

An iterative splitting

$$(1-\mathrm{e}^{-a\,x})^i = (1-\mathrm{e}^{-a\,x})^{i-1}\,(1-\mathrm{e}^{-a\,x}) \tag{30}$$

results in a summation of integrals of the type

$$\int_0^{\mathrm{N}}(1-\mathrm{e}^{-a\,x})^{i-1}\,\mathrm{e}^{-a\,x}\mathrm{d}x = \frac{1}{a\,i}\cdot \tag{31}$$

Thus, we obtain

$$\langle P^{\max}(L)\rangle = \sum_{i=1}^{L}\frac{1}{a\,i}\cdot \tag{32}$$

A restriction of the statistics to values of the pressure $P > 1000$ g cm s^{-2}, performing an analogous calculation, results in

$$\langle P^{\max}(L)\rangle = \sum_{i=1}^{L}\frac{1}{a\,i} + 1000\text{ g cm s}^{-2}. \tag{33}$$

From the simulations we extracted the pressure distribution yielding – as expected – an exponential decrease. The prefactor is $a = 0.0009$ for $\Omega = 10$ Hz and $a = 0.001$ for $\Omega = 2$ Hz. The corresponding curves are plotted in Figure 10 as dotted lines and reasonably describe the measured values. Thus, we indirectly can conclude from the measurement that we have an exponential distribution, which indicates the occurrence of force chains.

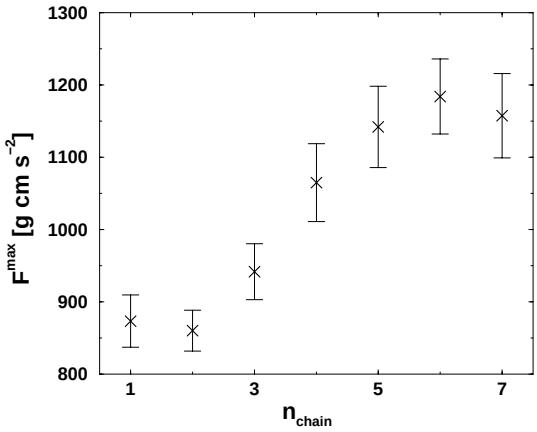

Fig. 11. The maximal force acting on a particle as a function of the relative position in the force chain. The monotonous behaviour indicates that forces are accumulating downwards along the chain.

Further insight into the mechanism of force chains is achieved through Figure 11 which shows the average of the maximal force acting on a grain as a function of its position within the force chain. The average was performed for all force chains of length $L = 8$. The top particle of a chain, corresponding to the maximal y-coordinate, was defined as position 1. The monotonous increase of this maximal force indicates that, on average, strain accumulates downwards along the force chain. In this respect a force chain is similar to a beam in a framework: The masses and momenta of all particles above a force chain are supported by this chain, with the consequence that lower particles of the chain are heavier loaded than upper ones. This trend is clearly visible in the data of Figure 11. Furthermore, a force chain can shield neighbouring particles, *i.e.* these grains experience a much weaker force which can be observed in the simulation data as well.

Figure 12 shows the spatial pressure distribution for different rotation velocities. Here grey values code the *absolute* local pressure, with light pixels indicating low and dark pixels high values, in order to allow for a direct comparison of all three images.

The presented data are temporal averages. To extract the spatial distribution of this data, the two-dimensional space was coarse-grained. For each time step the positions of all particles were mapped to the grid and the resulting instantaneous local pressure was added to its related cell. Notice that the averaged data does not reflect the occurrence of force chains.

Surprisingly, for lower rotation velocities one finds that direct impacts with high relative velocities at the material surface do not result in high local pressure. Therefore, these impacts are not relevant for the fragmentation of grains in ball mills. Regions of high pressure can be found mainly near to the wall, deep inside the material. This observation is in good agreement with the experimental result of Rothkegel and Rolf [1,2]. The extreme right figure in Figure 12 reveals a different behaviour. The maximum

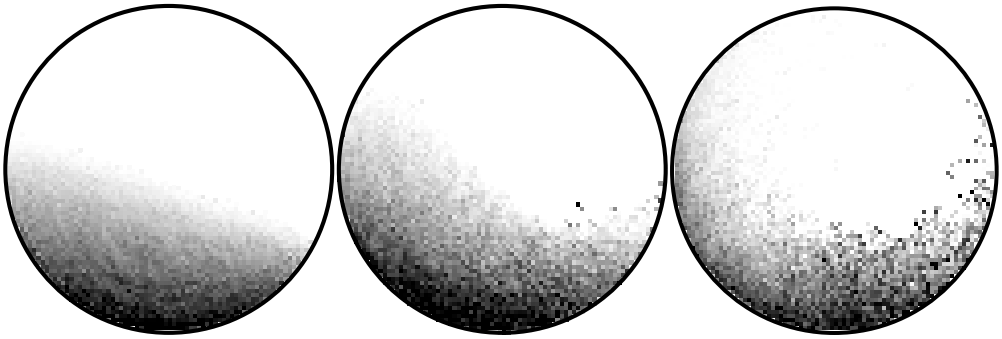

Fig. 12. Spatial distribution of the pressure. Grey values code the absolute pressure, with light pixels indicating low and dark pixels high pressure values. The grey scale is unique for all three figures to allow for a direct comparison. From left to right: $\Omega = 2$ Hz, $\Omega = 10$ Hz, $\Omega = 19$ Hz. While for lower rotation velocities the maximum is deep inside the material near to the wall, for higher rotation velocity it is near to the free surface, which is heavily agitated by impacts.

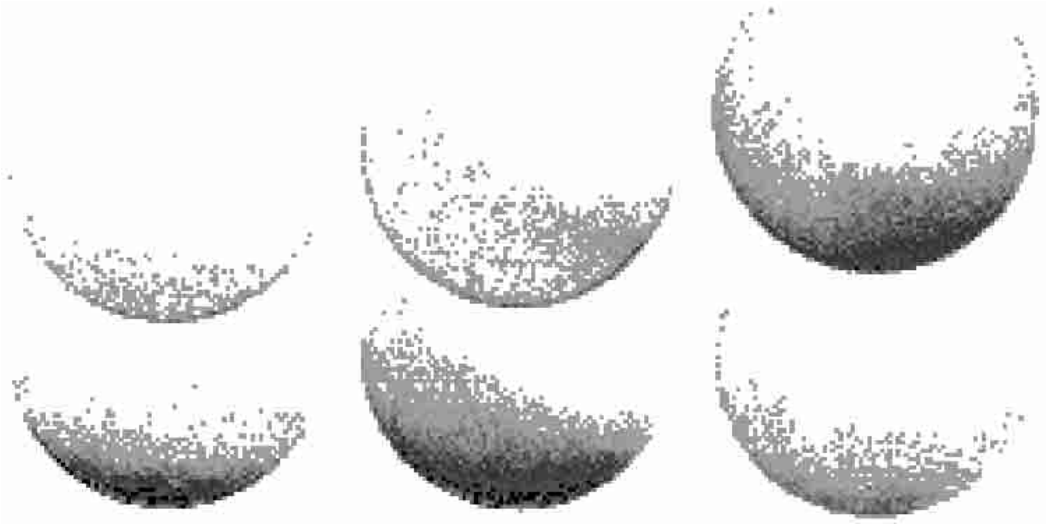

Fig. 13. Spatial frequency distribution of particles, exerted to a pressure $P > 3000$ g cm s^{-2}. Grey values, unique throughout the images, code the frequency: dark pixels high frequency and light pixels low frequencies. The top row only accounts for particles which do not belong to a force chain while, in contrast, the bottom row includes only particles being member of a force chain. From left to right: $\Omega = 2$ Hz, $\Omega = 10$ Hz, $\Omega = 19$ Hz. By visual inspection it becomes obvious that most of the heavier loaded particles belong to force chains and are found near to the wall of the mill.

is near to the material surface where heavy impacts occur. The absolute values of the pressure are much lower than in the left figures. This observation relates to the existence of rather weak force chains.

Figure 13 shows the spatial distribution of the number of particles, which experience a pressure $P_i >$ 3000 g cm s^{-2}. In these figures the particles which belong to a force chain are only considered in the bottom row whereas particles not belonging to a force chain are contained in the top row. Figures 13 can be directly compared with the figures of Rothkegel [1] (see Fig. 8); both are found to be in good agreement. The maxima of the distribution for Ω_{I} and Ω_{II} lie near to the wall of the mill, inside the material as observed in the experiment. Those maxima are an exclusive result of force chains. Grains not belonging to a force chain contribute only weakly to the comminution. For the higher velocity Ω_{III} direct impacts of particles at the surface are the dominant part. Nevertheless, absolute values are much lower than for Ω_{I} and Ω_{II}. Again, this observation is in good agreement with the experiment [1].

6 Conclusion

We have simulated the process of autogenous dry comminution in a ball mill by the method of molecular dynamics. To this end we developed a novel algorithm which

accounts for fragmentation of particles. Throughout our simulations all particles, including the fragments, were modelled as spheres. To accomplish this idealization we introduced rather short-lived unphysical transient situations in which the fragments resulting from a cracked particle penetrate each other. The results of our simulations are available in the internet as animated sequences under `http://summa.physik.hu-berlin.de/~kies/mill/bm.html`

Employing our molecular dynamics algorithm we could satisfactorily reproduce experimental phenomena, *e.g.* the normalized comminution rate as a function of the normalized rotation speed and the spatial pressure distribution.

From the achieved numerical data we were able to explain an experimental result which was poorly understood so far [1]: Comminution processes in ball mills occur deep inside the material rather than close to the surface where the relative collision velocity is maximal. We explained this effect by the formation of force chains. Particles which are members of one or more force chains experience a significantly larger average force, thus substantially enhancing the fragmentation probability, as compared to particles which do not belong to any force chain.

From this we concluded that the experimentally observed and numerically achieved spatial pressure and fragmentation distributions are crucially determined by the formation of force chains. Direct collisions of particles are of minor importance for comminution. Without the existence of force chains ball mills would work much less efficient. In the context of a ball mill efficiency optimization it would be intriguing to investigate the possibility of enhancing the formation of force chains, *e.g.* by modifications of the geometrical properties of mills, additional application of vibration etc.

The method developed in this article may be elaborated in many different aspects:

- The numerical investigations were done in two dimensions. Ball mills are three-dimensional devices.
- Axial transport of the material was not simulated.
- All particles, including fragments, were spherical.
- Only a single-level process was simulated. Modern ball mills frequently operate in multi-level mode.
- Adhesive forces were not considered in the force law.
- Variation of material properties which originates from an increase of temperature due to comminution was not considered.

We expect that molecular dynamics will rapidly develop towards an important tool for the powder technology machinery. Due to the rapid progress in hardware and software technology, including parallel algorithms, it will soon be possible to construct and optimize powder technology facilities.

The authors thank S. Bernotat, R. Drögemeier, E. Gommeren, G. Gudehus, H.J. Herrmann, L. Rolf, J. Schwedes and R. Weichert for discussion and for providing relevant literature. The work was supported by German Science Foundation through project Po472/3-2.

References

1. B. Rothkegel, *Örtliche Verteilung der Stoßenergien ≥ 22 mJ und die zugeordneten Bewegungszustände von Modellmahlkörpern in einer Modellkugelmühle*, Ph.D. thesis, Technical University Berlin, 1992.
2. L. Rolf (personal communication).
3. P.K. Haff, B.T. Werner, Powder Technol. **48**, 239 (1986).
4. P.A. Cundall, O.D.L. Strack, Géotechnique **29**, 47 (1979).
5. J.A.C. Gallas, H.J. Herrmann, S. Sokołowski, Phys. Rev. Lett. **69**, 1371 (1992).
6. Y.-h. Taguchi, Phys. Rev. Lett. **69**, 1367 (1992).
7. O.R. Walton, in *Numerical Methods in Geomechanics*, edited by Z. Eisenstein (Balkema, Rotterdam, 1982).
8. O.R. Walton, R.G. Braun, in *Joint DOE/NSF Workshop on flow of particulates and fluids* (Ithaka, 1993), pp. 1-17.
9. V. Buchholtz, T. Pöschel, in *Friction, Arching and Contact Dynamics*, edited by D.E. Wolf, P. Grassberger (World Scientific, Singapore, 1997), p. 265.
10. J.A.C. Gallas, H.J. Herrmann, T. Pöschel, S. Sokołowski, J. Stat. Phys. **82**, 443 (1996).
11. G.A. Kohring, Physica A **195**, 1 (1993).
12. C. Salueña, S.E. Esipov, T. Pöschel, S. Simonian, SPIE **3327**, 19 (1998).
13. C. Salueña, S.E. Esipov, T. Pöschel, Phys. Rev. E **59**, 4422 (1999).
14. G.A. Kohring, S. Melin, H. Puhl, H.-J. Tillemans, W. Vermöhlen, Appl. Mechanics Eng. **124**, 273 (1995).
15. T. Yokohama, K. Tamura, G. Jimbo, Intern. Chem. Eng. **34**, 611 (1994).
16. T. Yokohama, K. Tamura, G. Jimbo, in *Proceedings 8. European Symposium on Comminution*, edited by E. Forssberg (Elsevier, Amsterdam, 1996), p. 413.
17. P.K. Songfack, S. Agrawala, B.K. Mishra, R.K. Rajamani, in *Proc. 2nd Intern. Conf. on Discrete Element Methods*, edited by J.R. Williams, G.G.W. Mustoe (IESL, Cambridge, 1993), p. 205.
18. A tumbling ball mill is a tubular vessel which is kept rotating around its own axis. The grinding medium, here balls, is elevated by the vessel wall and then rolls, slides, or falls toward the lowest point of the vessel. The feed material is trapped between the media particles and, thus, ground by their movement. In case the grinding media is the feed material itself one speaks of autogeneous grinding. Even though the autogeneous comminution in a tumbling mill is considered throughout this paper we, nevertheless, will use the simple term ball mill.
19. H. Hertz, J. Reine Angewandte Math. **92**, 156 (1882).
20. L.D. Landau, E.M. Lifschitz, *Elastizitätstheorie* (Akademie Verlag, Berlin, 1983).
21. P.A. Engel, *Impact Wear of Materials* (Elsevier, Amsterdam, 1976).
22. M.P. Allen, D.J. Tildesley, *Computer Simulations of Liquids* (Clarendon Press, Oxford, 1987).
23. J. Schäfer, S. Dippel, D.E. Wolf, J. Phys. France I **6**, 5 (1996).
24. N.V. Brilliantov, F. Spahn, J.-M. Hertzsch, T. Pöschel, Phys. Rev. E **53**, 5382 (1996).
25. R. Ramírez, T. Pöschel, N.V. Brilliantov, T. Schwager, Phys. Rev. E **60**, 4465 (1999).
26. D.C. Rapaport, J. Comp. Phys. **34**, 184 (1980).

27. T. Schwager, T. Pöschel, Phys. Rev. E **57**, 650 (1998).
28. S. Luding, S. McNamara, Granular Matter **1**, 113 (1998).
29. R. Weichert, Zement Kalk Gips **45**, 1 (1992).
30. R. Weichert, Int. J. Mineral Processing **22**, 9 (1988).
31. W. Weibull, *The Phenomenon of Rupture in Solids. Proc. 151 and 153. Ing. Vetensk. Akad.* (Stockholm, 1939).
32. S. Bernotat, K. Schönert, Size reduction, *Ullmann's Encyclopedia of Industrial Chemistry B2*, 1 (1988).
33. F. Kun, H.J. Herrmann, Int. J. Mod. Phys. **7**, 837 (1996).
34. F. Kun, H.J. Herrmann, Comp. Meth. Appl. Mech. Eng. **138**, 3 (1996).
35. R. Schuhmann, *Am. Inst. Mining, Met.*, Petrol. Engrs. Tech. Publ. No. 1189 (1940).
36. P. Rosin, E. Rammler, J. Inst. Fuel **7**, 29 (1933).
37. J.J. Gilvary, J. Appl. Phys. **32**, 391 (1961).
38. J.J. Gilvary, B.H. Bergstrom, J. Appl. Phys. **32**, 400 (1961).
39. J.A. Herbst, M. Siddique, K. Rajamani, E. Sanchez, Soc. Min. Eng. AIME Trans. **272**, 1945 (1981).
40. J.A. Åström, H.J. Herrmann, Eur. Phys. J. B **5**, 551 (1998).
41. A.N. Kolmogorov, Doklad. Akad. Nauk. S.S.S.R. **31**, 99 (1941).
42. P.R. Halmos, Ann. Math. Stat. **15**, 182 (1944).
43. B. Epstein, J. Franklin Inst. **244**, 471 (1947).
44. J. Leluschko, *Untersuchungen zum Einfluß der Flüssigkeit bei der Naßmahlung in Kugelmühlen*, Ph.D. thesis, Techn. Universität München, 1985.
45. The term pressure distribution does not relate to the spatially averaged force vector field, but to the absolute value of forces acting between particles. Strictly speaking, this quantity has the unit of a force, however, to avoid confusion with the averaged force vector field we adopt the term pressure from engineering literature.
46. J. Rajchenbach, Phys. Rev. Lett. **65**, 2221 (1990).
47. J. Duran, T. Mazozi, S. Luding, E. Clément, J. Rajchenbach, Phys. Rev. E **53**, 1923 (1996).
48. R. Behringer, Nonlinear Science Today **3**, 1 (1993).
49. C.H. Liu, S.R. Nagel, D.A. Schecter, S.N. Coppersmith, S. Majumdar, O. Narayan, T.A. Witten, Science **269**, 513 (1995).
50. P. Dantu, Ann. Ponts Chausses **4**, 144 (1967).
51. S. Schöllmann, Phys. Rev. E. **59**, 889 (1999).
52. S.E. Esipov, T. Pöschel, J. Stat. Phys. **86**, 1385 (1997).
53. D.E. Wolf, in *Computational Physics*, edided by K.H. Hoffmann, M. Schreiber (Springer, Heidelberg, 1996), p. 64.
54. D. Howell, B. Miller, C. O'Hern, R.P. Behringer, in *Friction, Arching and Contact Dynamics*, edided by D.E. Wolf, P. Grassberger (World Scientific, Singapore, 1997), p. 293.
55. F. Radjai, M. Jean, J.J. Moreau, S. Roux, Phys. Rev. Lett. **77**, 274 (1996).